Chem Rev Lett 8 (2025) 1003-1017

Research Article

Chemical Review and Letters
journal homepage: www.chemrevlett.com
ISSN (online): 2645-4947 (print) 2676-7279

Pt-embedded pyrrolic and pyridinic N-doped graphene quantum dots as a viable aflatoxin B1 sensor: Insights from DFT calculations

Reza Behjatmanesh-Ardakani[1,] *, Hossein Mohammadi-Manesh[2], Masoud Sedaghatjo[3]

[1]*Department of Chemical Engineering, Faculty of Engineering, Ardakan University, P.O. Box: 184, Ardakan, Iran.*
[2]*Department of Chemistry, Faculty of Science, Yazd University, P.O. Box 89195-741, Yazd, Iran.*
[3]*Department of Chemistry, Payame Noor University (PNU), P.O. Box 19395-4697, Tehran, Iran.*

ARTICLE INFO

Article history:
Received 25 May 2025
Received in revised form 11 June 2025
Accepted 03 July 2025
Available online 03 July 2025

Keywords:
Aflatoxin B1
Pt-embedded
Graphene quantum dot
Pyrrolic nitrogen
Pyridinic nitrogen

ABSTRACT

Aflatoxin B1 is a well-established carcinogen, and even low concentrations pose significant health risks by increasing the likelihood of cancer development. Therefore, various sensors have been tested to identify the most effective adsorbents for its detection. In this study, pristine and Pt-embedded nitrogen-doped graphene quantum dot sensors were modeled to investigate their interactions with Aflatoxin B1 (AFB1). Two types of nitrogen doped graphene (pyrrolic and pyridinic ones) were examined to evaluate their potential as AFB1 sensors. Multiple configurations of AFB1 were considered for each sensor to calculate binding energies and changes in the HOMO-LUMO gap. Results indicate that without a Pt single atom, the average band gap change due to AFB1 adsorption on pristine pyrrolic N-doped graphene is only 3%, which is insufficient for effective sensing. The average binding energy between AFB1 and pyrrolic N-doped graphene is approximately −1.1 eV, indicating moderate interaction. In contrast, pyridinic N-doped graphene shows an average band gap change of less than 2% and a binding energy of about −0.5 eV. Introducing a Pt single atom significantly enhances performance: the average band gap changes increase by approximately 16% for pyrrolic and over 800% for pyridinic N-doped graphene. Correspondingly, their averaged binding energies with AFB1 increase to −1.5 eV and −2.7 eV, respectively. These findings suggest that Pt-embedded pyridinic N-doped graphene is a promising candidate for disposable AFB1 sensors. Additionally, various physicochemical parameters—including ionization potential, hardness, electrical conductivity, recovery time, chemical reactivity, and electrophilicity—were analyzed. The nature of interactions between AFB1 and the two Pt-embedded N-doped graphene sensors was further examined using quantum theory of atoms in molecules (QTAIM), while stabilities arising from intermolecular charge transfers were investigated via natural bond orbital (NBO) analysis. All noncovalent interactions were analyzed and visualized using noncovalent interaction (NCI) and reduced density gradient (RDG) methods.

1. Introduction

Aflatoxin B1 (AFB1) is classified as a Group 1 carcinogen and Group 2B potential carcinogen to humans [1]. Prolonged exposure to even very low concentrations of AFB1 significantly increases the risk of developing cancer, particularly hepatocellular carcinoma. After metabolic activation in the body, AFB1 retains strong mutagenic properties, contributing to DNA damage and the initiation of cancer [2]. Notably, AFB1 is highly stable and can persist through high-temperature food and animal feed processing, resulting in its presence in a wide range of products, including grains, animal feed, and dairy items, even after various processing steps. Currently, several detection technologies are used to identify AFB1 contamination, such as thin-layer chromatography (TLC), high-performance liquid chromatography (HPLC), mass spectrometry, and enzyme-linked immunosorbent assay (ELISA). However, each method has its limitations, and no single

* Corresponding author E-mail: behjatmanesh@ardakan.ac.ir
https://doi.org/10.22034/crl.2025.526157.1610

approach offers both rapid and simple detection while maintaining effectiveness under challenging conditions like high temperatures.

Recent advances have explored novel sensor and adsorbent materials for AFB1 detection and removal. For example, Xiulan et al. developed a gold nanoparticle–based antibody probe capable of detecting 2.5 ng/mL AFB1 within 10 minutes, although the sensor's preparation is time-consuming and costly [3]. Surface-enhanced Raman spectroscopy (SERS) has also been employed for AFB1 quantification; Lian et al. [4] and Gao et al. [5] demonstrated that SERS can detect AFB1 and analyze its interaction with gold and silver substrates, but the method requires specific, high-cost sample preparation and is sensitive to environmental conditions such as temperature and humidity. Additionally, Li et al. [6] utilized a covalent organic framework fiber membrane to adsorb AFB1, achieving 98% removal efficiency with at least 10 cycles of reuse, attributing the strong adsorption to π–π stacking, hydrogen bonding, and hydrophobic interactions. Samuel et al. [7] synthesized a zinc terephthalate metal-organic framework for AFB1 adsorption from water, finding that the adsorption kinetics followed a pseudo-second-order model and fit well with Langmuir and Freundlich isotherms.

Graphene and graphene oxide are widely utilized in the detection and adsorption of Aflatoxin B1 (AFB1). For instance, Li et al. developed an aptasensor incorporating gold nanoparticles and functionalized graphene oxide for the sensitive detection of AFB1, demonstrating notable stability and selectivity, and confirming its practical applicability in millet and corn samples [8]. However, aptasensors generally exhibit high sensitivity to changes in pH and temperature and tend to be less stable under elevated temperature and humidity conditions. Xia and coworkers introduced a method employing functionalized graphene hydrogel as a sensing platform, with luminol–palladium–graphene oxide serving as an electrochemiluminescence marker for AFB1 detection [9]. Ramalingam et al. presented a biochip based on a graphene quantum dot and gold composite for detecting trace amounts of AFB1 in milk; functionalization with gold nanoparticles enhanced electrical activity and reduced the limit of detection to below 4 nM [10]. Similarly, Mousavi and coworkers fabricated an electrochemical aptasensor from a graphene oxide and gold nanowire composite, utilizing changes in peak current during pulse voltammetry for AFB1 detection [11]. Numerous additional studies confirm the widespread use of graphene and graphene oxide in the fabrication of sensors and biosensors for AFB1 detection. Despite their effectiveness, these methods often involve complex procedures and time-consuming sample preparation. Therefore, there is an urgent need to design new catalysts that can be synthesized quickly and simply, while maintaining high stability at elevated temperatures. To minimize costs, it is advantageous to employ a rapid and inexpensive computational approach prior to synthesis to evaluate the adsorption and sensing capabilities of newly designed sensors for AFB1. In this context, density functional theory (DFT) is commonly used to model interactions between proposed sensors and AFB1, providing detailed microscopic insights into band gap changes and other properties during their interaction

DFT method has been widely used to study the electronic structures of nanomaterials and their interactions with contaminants and drugs [12-21]. In addition, DFT has also been employed to investigate the interactions between AFB1 and newly designed sensors. For instance, Lian and co-workers utilized DFT to study AFB1 adsorption on gold substrates, employing molecular electrostatic potential (MEP) mapping to identify potential docking sites [4]. Their frontier orbital calculations revealed charge transfer resonance excitation between AFB1's functional groups and gold, with observed Raman frequency shifts serving as a detection signal [4]. Other studies report weak AFB1 binding energies (0.2–0.26 eV) for covalent organic frameworks, where adsorption is primarily driven by hydrogen bonding and π–π stacking interactions [6]. Mo et al. combined non-equilibrium Green's function (NEGF) methods with ground-state DFT to model graphene-AFB1 systems, predicting a 3.167 μA current shift at 1.2 V bias upon AFB1 adsorption [22]. DFT simulations further suggest AFB1 protonation via water molecules at the lactone group's negatively charged oxygen, while its carbon atoms exhibit electrophilic behavior [23]. Additional studies have explored AFB1 interactions with clays [24], C_3–N_5 nanotubes [25], $B_{12}N_{12}$ nanocages [26], and C_{20} fullerenes [27].

Nitrogen-doped graphene has emerged as a promising sensor due to its active nitrogen sites. However, catalytic performance depends critically on nitrogen configuration. Pyrrolic and pyridinic nitrogen atoms introduce distinct electronic properties and structural features into the graphene lattice. Both configurations contain a carbon defect site, which serves as an anchoring point for transition metals such as platinum (Pt). In this study, we model the adsorption of AFB1 on Pt single-atom–anchored pyrrolic and pyridinic N-doped graphene and investigate the electronic properties of the resulting complexes. These properties are then systematically compared with those of pristine sensors to evaluate the influence of nitrogen configuration and Pt anchoring on AFB1 adsorption and sensing performance. The paper is as follows: First, pyrrolic and pyridinic N-doped graphene quantum dot sensors are constructed from the optimized periodic structures. These sensors are then further optimized. Next, the AFB1 molecule is optimized, and various initial configurations of AFB1 adsorbed on the surfaces of the graphene quantum dots are modeled and optimized. The electronic structures of the resulting

complexes are calculated, and the band gaps in the presence and absence of AFB1 are determined. By monitoring changes in the band gap, the potential of these catalysts as sensors is evaluated. In addition, charge transfer, the nature of the interactions, hardness, softness, Fermi level shifts, and other physicochemical parameters are also investigated and discussed.

2. Materials and Methods

A 6×6 supercell of graphene was used to construct the graphene quantum dot. The periodic supercell was converted to a non-periodic one, and all dangling bonds were capped with hydrogen atoms. Three carbon atoms were replaced by three nitrogen atoms to model N-doped graphene. Additionally, three and one more carbon atoms were removed from graphene to model pyrrolic and pyridinic nitrogen-doped graphene. To model graphene-supported single atom sensor, a Pt atom was added on top of the nitrogen atom cavity, and its position was optimized using DFT. Three different codes were employed for a detailed investigation of the interaction between AFB1 and the proposed sensors. First, the sensors, adsorbate, and all complexes were optimized using the PBE with a nonlocal version of many-body dispersion (MBD) [28-31] as implemented in the FHI-aims code [29-32]. The PBE functional is a widely used GGA functional that has been applied in various catalytic reaction simulations [33-37]. The optimized sizes of the N-doped graphene quantum dot supported Pt single atom sensors were 14.30 Å × 21.78 Å and 14.47 Å × 22.00 Å for pyrrolic and pyridinic types, respectively. The longest optimized diameter was observed for the pyridinic N-doped graphene quantum dot supported Pt single atom sensor. The optimized structures are shown in Figure 1 and 2. During FHI-aims calculations, all electrons (the full potential model) for all atoms, including Pt, were considered in constructing the wavefunction. The standard parameters of '*light'* model in FHI-aims code were used for all atoms [32]. '*Spin-unrestricted*' and '*atomic ZORA scalar*' options were selected for all GGA and hybrid calculations. For SCF convergence and geometry optimizations, tolerances of 10^{-5} eV for total energy and 0.05 eV/Å for force were applied. The M06-2X method, a hybrid model with 54% HF exact exchange, was used for band gap calculations [38]. The Gaussian code [39] was also used for single-point post-processing calculations to generate the wavefunction and to study natural bond orbitals via NBO 6.0 code [40]. The Multiwfn program was used for quantum theory of atoms-in-molecules (QTAIM) analyses and RDG calculations [41]. All RDG and QTAIM graphs were rendered using the VMD program [42], and all other graphs were prepared by GaussView [43].

In addition to the band gaps, various parameters including ionization potential (I), electron affinity (A), absolute electronegativity (χ), chemical potential (μ), absolute hardness (η), electrophilicity (ω) and maximum charge acceptance (ΔN_{max}) were also calculated. These parameters are commonly used as chemical reactivity descriptors and are valuable for understanding chemical compounds in detail and for developing artificial intelligence models for chemical reactions. The following formulas were used for these descriptors [44-46]:

$$I = -E_H \quad (1)$$

$$A = -E_L \quad (2)$$

$$E_{gap} = E_L - E_H = I - A \quad (3)$$

$$\chi = -\mu = -\left(\frac{\partial E}{\partial N}\right) \approx \frac{I+A}{2} \quad (5)$$

$$\eta = \frac{1}{2}\left(\frac{\partial^2 E}{\partial N^2}\right) = \left(\frac{\partial \mu}{\partial N}\right) \approx \frac{I-A}{2} = \frac{E_{gap}}{2} \quad (4)$$

$$\omega = \frac{\mu^2}{2\eta} \quad (6)$$

$$\Delta N_{max} = \frac{I+A}{I-A} \quad (5)$$

In these formulas, E_H is the energy of the highest occupied molecular orbital (HOMO) and E_L is the energy of the lowest unoccupied molecular orbital (LUMO). For materials with a band gap, such as insulators and semiconductors, the Fermi level cannot be precisely located, and any point between HOMO and LUMO can be considered as the Fermi level.

To investigate the sensing performance of the proposed sensors, the electrical conductivity (σ) was also calculated. The electrical conductivity can be related to the band gap by following relation [47]:

$$\sigma = AT^{3/2}\exp\left(\frac{-E_{gap}}{2kT}\right) \quad (6)$$

Where T is the absolute temperature, k is Boltzmann's constant, and A is a constant. A smaller band gap corresponds to higher electrical conductivity. A larger change in electrical conductivity is expected to produce a more detectable electrical signal and more effective AFB1 detection. The relative electrical conductivity can be calculated with comparing the data for the complexes data and the pristine sensors:

$$\%\sigma = \frac{\sigma_{complex}}{\sigma_{pristine}} = \exp\left(\frac{-\left(E_{gap}^{complex} - E_{gap}^{pristine}\right)}{2kT}\right) = \exp\left(\frac{-\Delta E_{gap}}{2kT}\right) \quad (7)$$

Here, the references for complexes A and B are the first pristine pyrrolic and pyridinic N-doped graphene sensors (without Pt single atom; see Table 1), and the references for other complexes are the second pristine N-doped sensors (Pt-embedded ones; see Table 1). Recovery time (τ) is another important parameter, evaluated by the following equation:

$$\tau = \upsilon_0^{-1}\exp\left(\frac{E_{ads}}{kT}\right) \quad (8)$$

Where ν_0 is the attempt frequency and E_{ads} is the adsorption energy. The attempt frequency is in the range of 10^{12}–10^{14} Hz. Considering order of 1000 cm^{-1} for $C-C$ and $C=C$ vibrations in graphene and the G-band in Raman spectra, ν_0 is approximately $\mathcal{O}(\nu_0) \approx 10^{13}$ Hz.

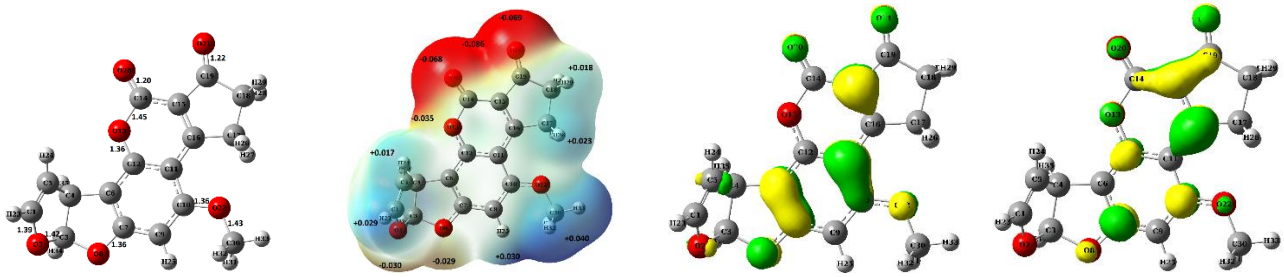

Fig. 1. Optimized structure of AFB1 calculated at the PBE+MBD/light level of theory using the FHI-aims code. Molecular electrostatic potential (in atomic units, a.u.) calculated via the Gaussian code. HOMO and LUMO iso-surfaces (density: 0.05 a.u.) are shown for electronic structure analysis.

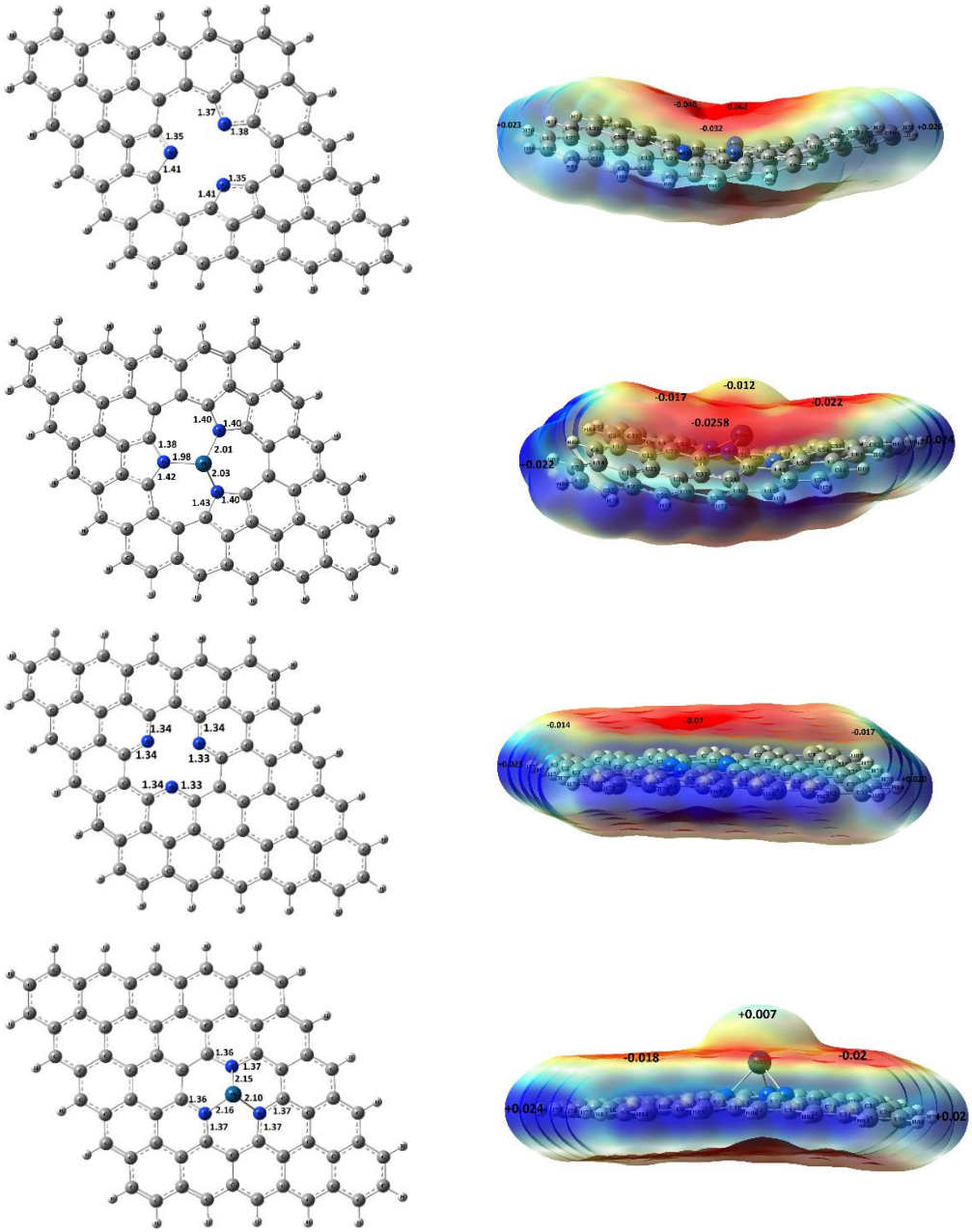

Fig. 2. Optimized structures of pristine and Pt-embedded pyrrolic (top) and pyridinic (bottom) N-doped graphene quantum dot sensors calculated at the PBE+MBD/light level of theory using the FHI-aims code. Molecular electrostatic potential (MEP, in atomic units, a.u.) calculated via the Gaussian code. Positive values (blue regions) indicate electrophilic sites, while negative values (red regions) indicate nucleophilic sites.

Table 1. The quantum chemical descriptors for pristine and complex forms of pyrrolic N-doped graphene, both with and without Pt atom. All values are in eV except for $\%\Delta E_{gap}$ and ΔN_{max}.

Compound	I	A	E_{gap}	$\%\Delta E_{gap}$[1]	μ	η	ω	ΔN_{max}
First Pristine[2]	5.75	3.69	2.06	—	−4.72	1.03	10.80	4.58
Complex A	5.88	3.87	2.01	−2.43	−4.88	1.01	11.83	4.85
Complex B	5.77	3.73	2.03	−1.46	−4.75	1.02	11.08	4.67
Second Pristine[3]	5.46	3.56	1.90	—	−4.51	0.95	10.73	4.76
Complex C	4.72	3.36	1.36	−28.42	−4.04	0.68	12.00	5.94
Complex D	4.86	3.31	1.55	−18.42	−4.08	0.77	10.75	5.27
Complex E	5.19	3.73	1.46	−23.16	−4.46	0.73	13.59	6.10
Complex F	5.18	3.56	1.62	−14.74	−4.37	0.81	11.81	5.40
Complex G	5.33	3.31	2.02	+6.32	−4.32	1.01	9.22	4.27

[1]The value of $\%\Delta E_{gap}$ is calculated by $100\times\left|\left(\frac{E_{gap}^{complex}-E_{gap}^{pristine}}{E_{gap}^{pristine}}\right)\right|$. [2]pyrrolic N-doped graphene without Pt atom. [3]Pt-embedded pyrrolic N-doped graphene.

3. Results and Discussion

3.1. Geometrical structures and the adsorption details

Figure 1 and 2 present the optimized structures of AFB1 and both pristine pyrrolic and pyridinic N-doped graphene quantum dots, with and without a single Pt atom. The pyrrolic N-doped graphene quantum dot exhibits a curved structure, a feature that is partly retained even after Pt embedding. This curvature is illustrated in Figure 3, which provides side-view snapshots of the sensors. Structural analysis reveals that the C–N bond length in pristine pyrrolic N-doped graphene is longer than in the pristine pyridinic counterpart. Specifically, C–N bonds in pyrrolic N-doped graphene range from 1.35 to 1.41 Å, while those in pyridinic N-doped graphene are between 1.33 and 1.34 Å. Upon Pt embedding in the cavity, the C–N bond lengths increase, attributed to the stronger electron-donating ability of Pt compared to carbon, which leads nitrogen atoms to preferentially interact with Pt and weakens their bonds with carbon.

The pyridinic N-doped graphene structure is more symmetrical, with more uniform C–N bond lengths, whereas the pyrrolic form is more twisted and shows greater variation in these bonds. Additionally, the Pt atom is positioned closer to the nitrogen atoms in the pyrrolic structure than in the pyridinic one. Compared to the pyridinic structure, the Pt is closer to the nitrogen atoms in the pyrrolic structure. This results in the Pt atom being farther from the graphene plane in the pyridinic structure, providing more space for interaction with AFB1. In the pyrrolic N-doped graphene, the interaction between nitrogen atoms and Pt leads to the formation of three five-membered and three seven-membered rings, while in the Pt-embedded pyridinic N-doped graphene, all rings are six-membered.

Figure 1 and 2 also display the molecular electrostatic potential (MEP) maps of the studied compounds. Negative and positive electrostatic potentials are shown in red and blue, respectively, with the values (in atomic units) indicated near key atoms. For AFB1 (Figure 1), all oxygen atoms exhibit negative electrostatic potentials, with those in the α-pyrone and cyclopentenone groups showing the most negative values (approximately −0.07 a.u.). For the sensors without Pt, negative electrostatic potential is observed near the center of the quantum dots, with average values above nitrogen atoms of −0.05 a.u. for pyrrolic and −0.07 a.u. for pyridinic N-doped graphene. The introduction of Pt modifies both the geometry and the electrostatic potential above the Pt atom: in pyrrolic and pyridinic N-doped graphene, these values are −0.012 a.u. and +0.007 a.u., respectively, both more positive than in the Pt-free sensors. However, a stronger coordination interaction between the pyridine nitrogen and platinum center is evident, as demonstrated by molecular modeling studies and experimental observations of chelate formation dynamics. These findings suggest that, in the absence of Pt, AFB1 interacts mainly via its hydrogen atoms or through π–π stacking. When Pt is present, AFB1 preferentially interacts with the sensors via its oxygen atoms. For both sensor types, the interaction between Pt and the oxygens of α-pyrone and cyclopentenone in AFB1 yields the highest binding energies, calculated as −2.39 eV for the pyrrolic and −3.79 eV for the pyridinic systems.

AFB1 consists of 35 atoms and features multiple functional groups, enabling it to adopt a variety of conformations upon interaction with the studied sensors. The distribution of its HOMO and LUMO extends across the entire molecule (see Figure 1), allowing all atoms to potentially participate in interactions with electron donor and acceptor groups. To comprehensively explore possible adsorption modes, initial configurations for the complexes were generated by positioning each functional group of AFB1 near the reactive centers of the N-doped graphene sensors. Optimization of several of these starting geometries led to converged structures exhibiting similar geometrical arrangements and binding energies. Figures 4–7 summarize the various optimized structures of AFB1 adsorbed on the surfaces of pyrrolic and pyridinic N-doped graphene quantum dots, both with and without a single Pt atom.

Fig. 3. Side views of the optimized structures of pristine and Pt-embedded pyrrolic N-doped graphene quantum dot sensors calculated at the PBE+MBD/light level of theory using the FHI-aims code.

E_b (A)= −1.42 eV E_b(B) = −0.7 eV

Fig. 4. Two local minima on the potential energy surface (PES) of the AFB1–pyrrolic N-doped graphene complex. Structures were optimized at the PBE+MBD/light level of theory using the FHI-aims code. Configurations with oxygen near nitrogen sites were unstable and relaxed into these geometries. Binding energies were calculated at the M06-2X/light level. Hydrogen atoms (except those involved in hydrogen bonds) are omitted for clarity.

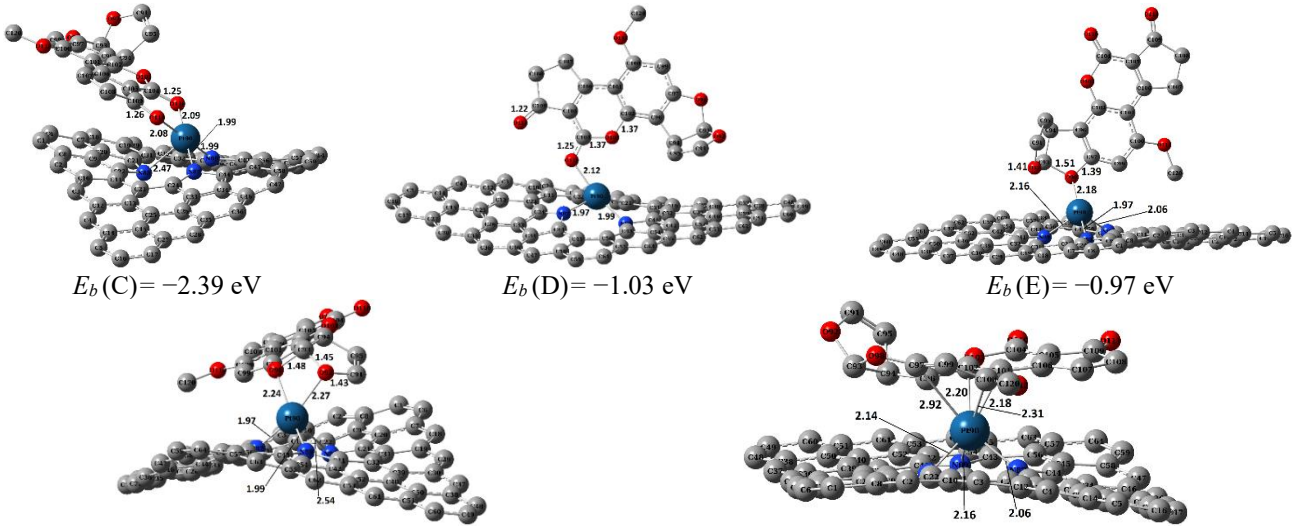

E_b (C)= −2.39 eV E_b (D)= −1.03 eV E_b (E)= −0.97 eV

E_b (F)= −1.51 eV E_b(G) = −1.71 eV

Fig. 5. Five optimized configurations of the AFB1···Pt-embedded pyrrolic N-doped graphene complex. Structures were optimized at the PBE+MBD/light level of theory using the FHI-aims code. Binding energies were calculated at the M06-2X/light level. Hydrogen atoms are omitted for clarity.

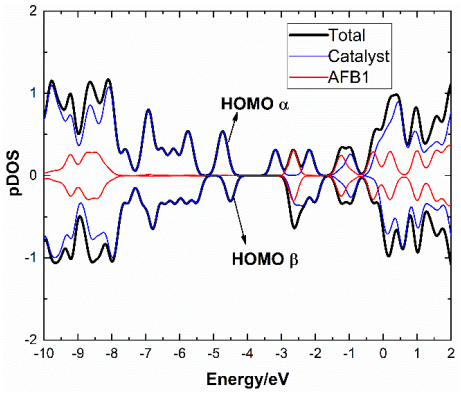

Fig. 6. Total and partial density of states (DOS) for complex C of Pt-embedded pyrrolic N-doped graphene. In the spin-up channel, both the HOMO and LUMO are localized on the sensor, whereas in the spin-down channel, the HOMO is on the sensor and the LUMO is on the AFB1 molecule (see also Figure Supp. 1).

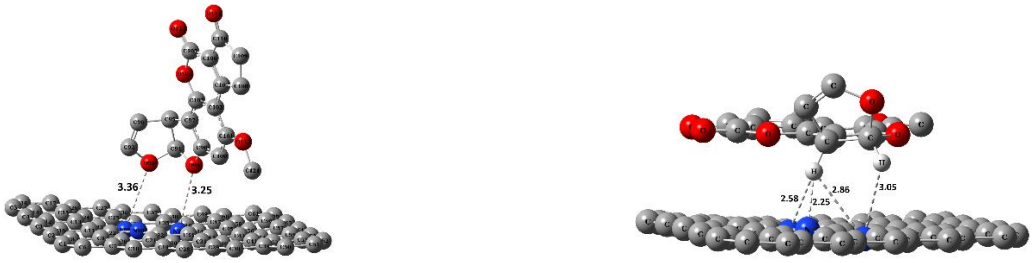

E_b(A) = −0.47 eV E_b(B) = −1.42 eV

Fig. 7. Two local minima on the potential energy surface (PES) of the AFB1·pyridinic N-doped graphene complex. Structures were optimized at the PBE+MBD/light level of theory using the FHI-aims code. Other configurations converged to these minima. Binding energies were calculated at the M06-2X/light level. Hydrogen atoms are omitted for clarity.

Figure 4 illustrates that different initial configurations of AFB1 on pristine pyrrolic N-doped graphene (without Pt) converge to two distinct optimized structures, labeled A and B, with the binding energies of E_b (A)= −1.42 eV and E_b(B) = −0.7 eV. The optimized geometries reveal that AFB1 preferentially adopts conformations enabling hydrogen bonding with pyrrolic nitrogen atoms. Configuration A exhibits hydrogen bond lengths of 2.44 Å and 2.34 Å, while configuration B shows lengths of 2.46 Å and 2.63 Å, consistent with moderate-strength hydrogen bonds. Notably, configuration A features parallel alignment between AFB1's benzene ring and the graphene surface (with a distance of 3.5 Å), facilitating π–π stacking, whereas configuration B adopts a perpendicular orientation lacking this interaction. The doubled binding energy of configuration A underscores its enhanced stability compared to configuration B, emphasizing the critical role of π–π interactions in adsorption strength. Figure 5 presents five optimized configurations of AFB1 adsorbed on the surface of a Pt-embedded pyrrolic N-doped graphene quantum dot. Among these, configuration C exhibits the highest binding energy (Eb = −2.39 eV), where the Pt atom interacts with two oxygen atoms from the cyclopentadienone (O111) and α-pyrone (O110) groups of AFB1. The NBO (QTAIM) charges for O110 and O111 are −0.63 e (−1.15 e) and −0.60 e (−1.13 e), respectively, while the corresponding values for O92, O98, O103, and O112 are −0.59 e (−1.07 e), −0.56 e (−1.06 e), −0.51 e (−1.12 e), and −0.56 e (−1.12 e), respectively. In configuration C, AFB1 is tilted such that its benzene rings engage in π–π stacking interactions with the benzene rings of the graphene substrate. Similarly, configurations F and G, with binding energies of −1.51 eV and −1.71 eV, respectively, also display π–π stacking interactions. Summing the QTAIM atomic charges indicates a net charge of +0.17 e on AFB1 and −0.17 e on the sensor in complex C, demonstrating that AFB1 acts as an electron donor while the sensor serves as an electron acceptor. Figure 6 shows the total and partial density of states (DOS) for complex C, revealing that the sensor contributes more significantly to the HOMO and LUMO distributions. In the spin-up channel, both the HOMO and LUMO are localized on the sensor surface, while in the spin-down channel, the HOMO resides on the sensor and the LUMO on AFB1. Consequently, the sensor can function as both an electron donor and acceptor in further complex formation, whereas AFB1 can only act as an electron acceptor.

Figure 7 shows the optimized structures of AFB1 adsorbed on the surface of pyridinic N-doped graphene without a Pt single atom. In configuration A, the lone pairs of O93 and O99 interact with the lone pairs of nitrogen atoms, while configuration B features both hydrogen bonding and π–π stacking interactions. In configuration A, the distances between O99 and N91, and between O93 and N89, are 3.25 Å and 3.35 Å, respectively. In configuration B, the hydrogen bond lengths H126···N89, H126···N90, and H126···N91 are 2.25 Å, 2.86 Å, and 2.58 Å, respectively. The other hydrogen atom, H125, exhibits longer distances to the three nitrogen atoms (3.05 Å, 3.32 Å, and 4.5 Å) indicating weaker hydrogen bonding. The minimum C(sp^2)···C(sp^2) distance between AFB1 and the benzene ring of the sensor is 3.42 Å, confirming the presence of π–π stacking between the benzene rings of AFB1 and the sensor. Additionally, H122 (from the CH_3 group) is 3.01 Å from the benzene ring of the sensor, suggesting that H···π interactions also contribute to stabilizing configuration B. Embedding a Pt single atom in pyridinic N-doped graphene increases the binding energy by at least a factor of two. In configuration F, where O112 and O113 (oxygen atoms from cyclopentadienone and α-pyrone groups) simultaneously interact with Pt, the binding energy reaches −3.79 eV. Besides oxygen atoms, some carbon atoms of AFB1 also interact with the Pt atom. In configuration G (Figure 8 and 9), the π electrons of the benzene ring in AFB1 interact with Pt. The bond lengths between Pt and carbons C98, C103, and C104 are 2.22 Å, 2.27 Å, and 2.05 Å, respectively, indicating strong interactions. The minimum distance between carbons of the α-pyrone group and the benzene ring of the sensor is 3.5 Å, confirming π–π stacking interactions in configuration G. Consequently, the binding energy of configuration G, despite lacking oxygen-Pt interactions, is higher than those of configurations C and D, which involve one and two oxygen atoms interacting with Pt, respectively.

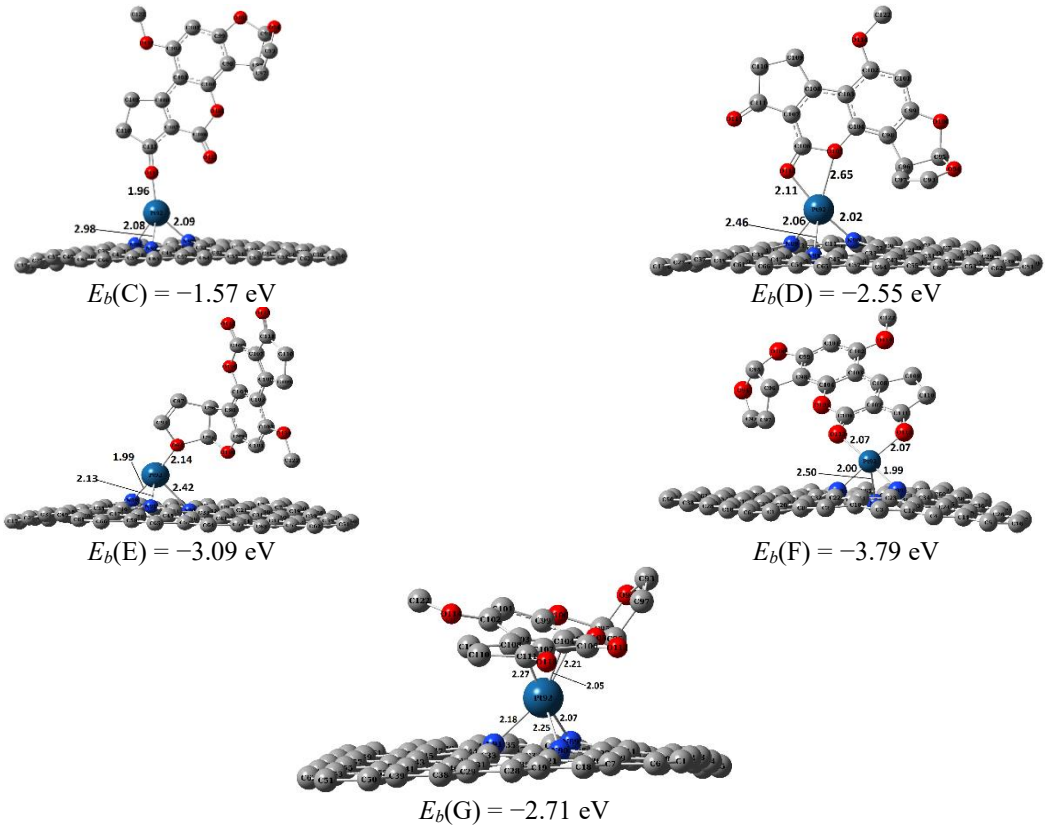

Fig. 8. Five optimized configurations of the AFB1···Pt-embedded pyridinic N-doped graphene complex. Structures were optimized at the PBE+MBD/light level of theory using the FHI-aims code. Binding energies were calculated at the M06-2X/light level. Hydrogen atoms are omitted for clarity.

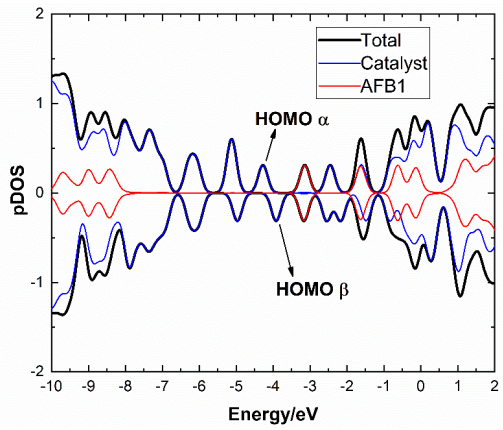

Fig. 9. Total and partial density of states (DOS) for complex F of Pt-embedded pyridinic N-doped graphene. In both spin-up and spin-down channels, the HOMO is localized on the sensor surface, while the LUMO is located on the AFB1 molecule (see also Figure Supp. 2)

3.2. Electronic and chemical-reactivity properties

Tables 1 and 2 summarize the band gap changes of pyrrolic and pyridinic N-doped graphene (with and without Pt) upon complexation with AFB1. When Pt is embedded in N-doped graphene, the value of ΔE_{gap} increases. The maximum percentage change in the band gap ($\%\Delta E_{gap}$) observed for pyrrolic- and pyridinic-N-doped graphene following complexation with AFB1 is 2.43% and 1.59%, respectively. These results suggest that these sensors alone lack sufficient sensitivity for AFB1 detection in sensor applications. However, supporting Pt on the surfaces of pyrrolic and pyridinic N-doped graphene leads to a significant increase in $\%\Delta E_{gap}$. The maximum $\%\Delta E_{gap}$ values for AFB1 complexation with Pt-embedded pyrrolic and pyridinic N-doped graphene quantum dots reach 28.42% (complex C) and 1286.67% (complex E), respectively. This suggests that Pt-embedded pyrrolic N-doped graphene is not an ideal AFB1 sensor, whereas Pt-embedded pyridinic N-doped graphene exhibits exceptional sensitivity and potential as an AFB1 sensor. For pristine Pt-embedded pyridinic N-doped graphene, the band gap is only 0.15 eV, indicating

metallic-like behavior. Upon complexation with AFB1, the band gap increases by approximately 13 times, transitioning the material to a semiconductor. This change implies that the electrical conductivity of Pt-embedded pyridinic N-doped graphene is, on average, reduced by more than 10^{20} times upon interaction with AFB1, making it a strong candidate for AFB1 sensing. Therefore, Pt-embedded pyridinic N-doped graphene is a suitable candidate as an AFB1 sensor. However, the average recovery time for Pt-embedded pyridinic N-doped graphene is relatively long ((~10^{50} s) due to its high binding energy with AFB1, suggesting its suitability as a disposable sensor.

A range of quantum descriptors including ionization potential (I), electron affinity (A), absolute electronegativity (χ), chemical potential (μ), absolute hardness (η), electrophilicity (ω), and maximum charge acceptance (ΔN_{max}) were calculated to further elucidate the reactivity of pristine N-doped graphene sensors and their AFB1 complexes. These descriptors also provide valuable data for future research involving neural networks or artificial intelligence (AI). Table 1 and 2 present these parameters for both pristine and complexes of pyrrolic and pyridinic N-doped graphene. For AFB1, the calculated parameters are I=5.75 eV, A=3.69 eV, E_{gap}=2.06 eV, μ=-4.8 eV, η=3.01 eV, ω=3.83 eV, and ΔN_{max}=1.59 eV. Since the ΔN_{max} of AFB1 is lower than that of pristine N-doped graphene (both pyrrolic and pyridinic), AFB1 acts as an electron donor when interacting with these sensors. This observation is consistent with the results from NBO, QTAIM, and electrophilicity analyses. The electrophilicity values of all pristine sensor forms are higher than that of AFB1, further supporting the conclusion that AFB1 behaves as an electron donor in these interactions. Comparative analysis of these quantum descriptors between AFB1 and the studied sensors indicates that the sensor's properties including ionization potential, electron affinity, chemical potential, absolute hardness, and electrophilicity differ significantly from those of AFB1, reinforcing their suitability as AFB1 sensors. These quantum descriptors are also promising candidates for input variables in neural network or other AI-based sensor researches.

3.3. NBO and QTAIM data

Natural Bond Orbital (NBO) analysis provides detailed insights into intermolecular and intramolecular charge-transfer interactions between AFB1 and the sensors. Table 3 and 4 summarize the most significant charge transfers involving donor (AFB1 oxygen orbitals) and acceptor (Pt-based orbitals) interactions for pyrrolic and pyridinic N-doped graphene systems, respectively. The second order perturbation energies ($E^{(2)}$) indicate the extent to which these charge transfers stabilize the complex. Only data with $E^{(2)}$ values greater than 20 kcal.mol^{-1} are presented in the tables. In all cases, donor orbitals originate from the oxygen atoms of AFB1, while the acceptor orbitals are associated with the Pt atom in the sensor. The three-dimensional iso-surface densities of the donor and acceptor orbitals are shown in Figure 10 and 11. The contribution of 'p' orbitals in donor orbitals is greater than that of sp^3 orbitals, and the nature of all acceptor orbitals is either the pure d orbitals of Pt atom or their hybridization with the Pt atom's 's' orbital. A high contribution of p-orbitals (>80%) in donor orbitals indicates the predominant role of p lone pairs in facilitating charge transfer interactions.

Table 2. Quantum chemical descriptors for pristine and complex forms of pyridinic N-doped graphene, both with and without a Pt atom. All values are in eV, except for $\%\Delta E_{gap}$ and ΔN_{max}.

Compound	I	A	E_{gap}	$\%\Delta E_{gap}$[1]	μ	η	ω	ΔN_{max}
Pristine[2]	5.60	3.09	2.51	—	−4.35	1.26	7.51	3.46
Complex A	5.80	3.25	2.55	+1.59	−4.52	1.28	8.02	3.54
Complex B	5.74	3.23	2.52	+0.40	−4.49	1.26	8.00	3.57
Pristine[3]	4.23	4.08	0.15	—	−4.15	0.08	114.92	55.33
Complex C	4.12	2.88	1.24	+726.67	−3.50	0.62	9.92	5.66
Complex D	4.34	2.81	1.53	+920.00	−3.57	0.76	8.35	4.68
Complex E	5.28	3.20	2.08	+1286.67	−4.24	1.04	8.66	4.09
Complex F	4.27	3.31	0.96	+537.58	-3.79	0.48	15.03	7.92
Complex G	4.42	3.40	1.02	+580.00	-3.91	0.51	15.03	7.92

[1]The value of $\%\Delta E_{gap}$ is calculated by $100\times\left|\left(\frac{E_{gap}^{complex}-E_{gap}^{pristine}}{E_{gap}^{pristine}}\right)\right|$. [2]pyridinic N-doped graphene without Pt atom. [3]Pt-embedded pyridinic N-doped graphene.

Table 3. Donor and acceptor orbitals, their hybridizations, and the second order perturbation theory analysis of the Fock matrix for pyrrolic N-doped graphene (complex C).

Donor	hybridization	acceptor	hybridization	$E^{(2)}$
$LP(2)_{O110}$	100% $(sp^{6.3})_O$	LV(1) Pt90	100%$(d)_{Pt}$	34.50
$LP(2)_{O110}$	100% $(sp^{6.3})_O$	LV(2) Pt90	100%$(sd^{0.07})_{Pt}$	20.2
$LP(2)_{O111}$	100% $(sp^{4.6})_O$	LV(1) Pt90	100%$(d)_{Pt}$	38.3
$LP(2)_{O111}$	100% $(sp^{4.6})_O$	LV(2) Pt90	100%$(sd^{0.07})_{Pt}$	22.0

Table 4. Donor and acceptor orbitals, and their hybridizations, and the second order perturbation theory analysis of the Fock matrix for pyridinic N-doped graphene (complex F).

Donor	hybridization	acceptor	hybridization	$E^{(2)}$
$LP(2)_{O112}$	100% $(sp^{5.7})_O$	LV(1) Pt92	100%$(d)_{Pt}$	38.4
$LP(2)_{O112}$	100% $(sp^{5.7})_O$	LV(2) Pt92	100%$(sd^{0.08})_{Pt}$	22.4
$LP(2)_{O113}$	100% $(sp^{4.5})_O$	LV(1) Pt92	100%$(d)_{Pt}$	38.5
$LP(2)_{O113}$	100% $(sp^{4.5})_O$	LV(2) Pt92	100%$(sd^{0.08})_{Pt}$	24.9

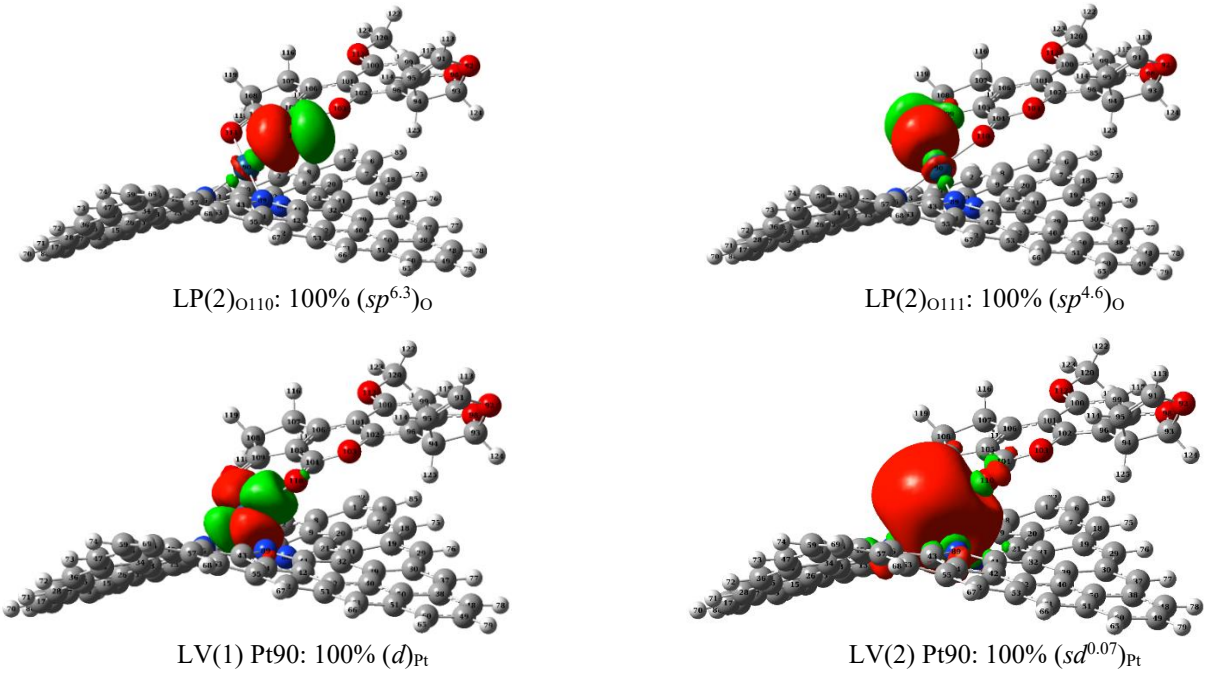

$LP(2)_{O110}$: 100% $(sp^{6.3})_O$ $LP(2)_{O111}$: 100% $(sp^{4.6})_O$

LV(1) Pt90: 100% $(d)_{Pt}$ LV(2) Pt90: 100% $(sd^{0.07})_{Pt}$

Fig. 10. Donor and acceptor orbitals for pyrrolic N-doped graphene. Detailed information is provided in Table 3. Lone pairs (LP) are electron donors, while lone valences (LV) serve as electron acceptors. The contribution of *p* orbitals in the donor orbitals exceeds 80%.

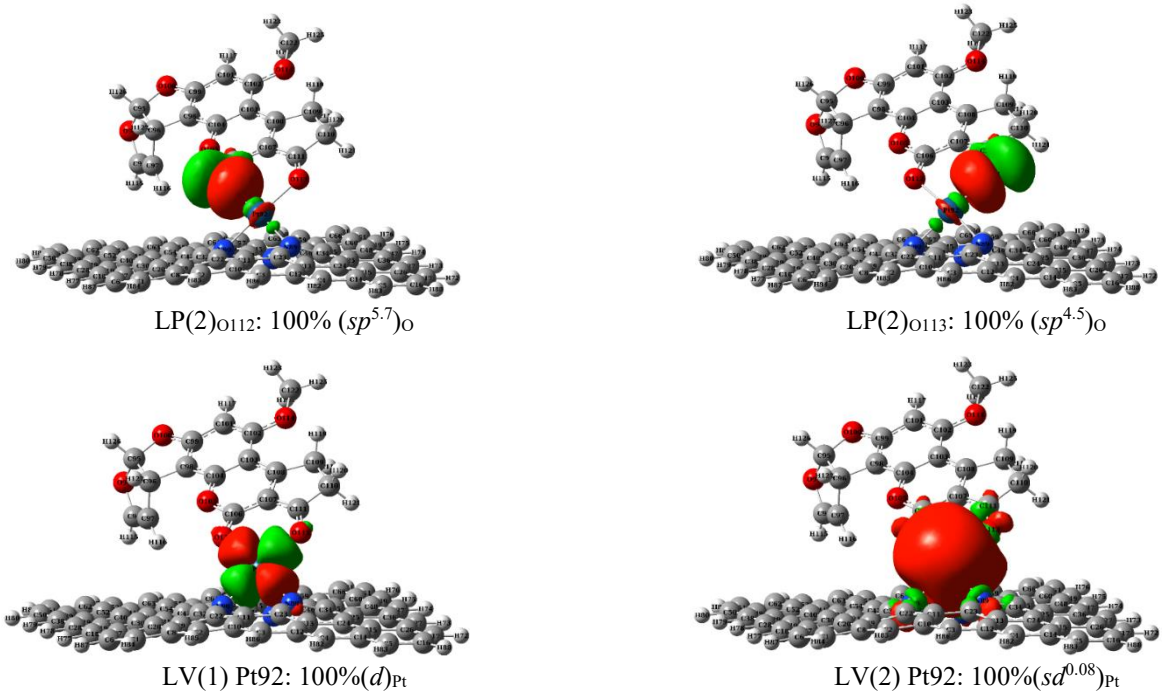

$LP(2)_{O112}$: 100% $(sp^{5.7})_O$ $LP(2)_{O113}$: 100% $(sp^{4.5})_O$

LV(1) Pt92: 100%$(d)_{Pt}$ LV(2) Pt92: 100%$(sd^{0.08})_{Pt}$

Fig. 11. Donor and acceptor orbitals for pyridinic N-doped graphene. Detailed information is provided in Table 4. Lone pairs (LP) act as electron donors, while lone valences (LV) serve as electron acceptors. The contribution of *p* orbitals in the donor orbitals exceeds 80%.

The NBO and QTAIM atomic charges of key atoms in complexes C and F of pyrrolic and pyridinic N-doped graphene are presented in Table 5 and 6, respectively. The total atomic charge on AFB1 is positive, with values of +0.17 |e| for the pyrrolic system and +0.20 |e| for the pyridinic system, while the corresponding total charges on the sensors are −0.17 |e| and −0.20 |e|, respectively. These charge distributions align with the NBO second-order perturbation analysis, electrophilicity, and ΔN_{max} values, collectively indicating that AFB1 acts as an electron donor and the sensors serve as electron acceptors in these complexes.

Topological and non-covalent interaction (NCI) graphs, together with reduced density gradient (RDG) data for pyrrolic (complex C) and pyridinic (complex F) complexes, are presented in Figure 12. The QTAIM parameters for key bond critical points (BCP) are reported in Table 7 and 8. QTAIM is suitable approach for elucidating the nature of intra- and intermolecular interactions. Table 7 lists all intermolecular (BCPs 2-7 and 11) and selected important intramolecular (BCPs 1, 8, 9, and 10) bond critical points for complex C, which consists of AFB1 interacting with pyrrolic N-doped graphene. BCPs 8, 9, and 10 all exhibit $\rho > 0.1, V \ll 0, \left|\frac{V}{G}\right| > 1,$ and $H < 0$, indicating that the bonds between Pt and N atoms in pyrrolic N-doped graphene are fully covalent [48]. The positive value of $\nabla^2\rho$ at these points demonstrates that charge concentration is located on the N atoms, consistent with the QTAIM and NBO charges in Table 5. BCPs 6 and 7, with $\rho = 0.08, V < 0, \left|\frac{V}{G}\right| \cong 1,$ and $H < 0$, reveal that both O110 and O111 in AFB1 form strong, partially covalent interactions Pt in the pyrrolic N-doped graphene. Other interactions listed in Table 7, characterized by $\rho \leq 0.01$ and $H > 0$, are closed shell in nature. Similarly, for complex F (AFB1 with pyridinic N-doped graphene), all interactions between the embedded Pt and N atoms are covalent. Both O113 and O114 (BCPs 3 and 4) display strong, partially covalent interactions with Pt, as indicated by their QTAIM parameters. The remaining interactions with $\rho \leq 0.01$ and $H > 0$, are closed shell interactions.

The NCI graphs in Figure 12 illustrate the three-dimensional distribution of interactions between AFB1 and the sensors. The geometry of AFB1 in complex C is more parallel to the sensor surface compared to complex F, resulting in pronounced π-π interactions in complex C that are absent in complex F. Conversely, H···C hydrogen bonds are stronger in complex F than in complex C.

RDG analysis, based solely on the electron density and its gradient, enables visualization of noncovalent interactions ranging from weak to strong. In RDG graphs, interactions are classified as attractive (blue), Van der Waals (green), and repulsive (red) [49]. The *y-axis* represents the reduced density gradient, while the *x-axis* corresponds to the product of the sign of λ_2 and electron density. For covalent and noncovalent bonds, the λ_2 is negative; for depletions such as steric repulsion, it is positive. Large positive RDG values correspond to regions far from the molecule, while small positive values near zero indicate bonding regions. Thus, spikes in the RDG graphs reflect the distribution of interactions within the complexes.

The RDG graphs in Figure 12 show that both complexes exhibit steric repulsive (red). In the *x* range of -0.05 to -0.03, both complexes display similar strong covalent bonding (chemical bonds in AFB1 and sensors). However, in the range between *x*= -0.03 and *x*=-0.01, complex F exhibits more Van der Waals interactions (green points with low RDG values). These Van der Waals interactions correspond to closed-shell interactions, ase discussed in the QTAIM section.

Table 5. NBO and QTAIM atomic charges for key atoms in complex C of pyrrolic N-doped graphene.

atom	NBO	QTAIM
N87	−0.53	−1.12
N88	−0.62	−1.09
N89	−0.54	−1.12
Pt90	+0.95	+0.96
O111	−0.60	−1.13
O110	−0.63	−1.15
O103	−0.51	−1.12

Table 6. NBO and QTAIM atomic charges for key atoms in complex F of pyridinic N-doped graphene.

atom	NBO	QTAIM
N89	−0.54	−1.25
N90	−0.52	−1.24
N91	−0.56	−1.26
Pt92	+0.92	+0.95
O112	−0.63	−1.15
O113	−0.60	−1.12

Table 7. QTAIM parameters for intra- and intermolecular interactions in complex C of AFB1 with Pt-embedded pyrrolic N-doped graphene.

Critical Point	ρ	$\nabla^2\rho$	V_r	G_r	H_r	$\lvert V_r \rvert / G_r$
1[O112···C107]	0.0107	0.0501	-0.0082	0.0103	0.0022	0.7884
2[H117···C8]	0.0055	0.0169	-0.0027	0.0035	0.0007	0.7873
3[C20···C105]	0.0072	0.0184	-0.0037	0.0041	0.0005	0.8860
4[C18···C102]	0.0057	0.0131	-0.0026	0.0029	0.0004	0.8764
5[H125···C29]	0.0068	0.0182	-0.0034	0.0040	0.0006	0.8578
6[O111···Pt90]	0.0868	0.5359	-0.1449	0.1383	-0.0065	1.0473
7[O110···Pt90]	0.0834	0.5304	-0.1400	0.1353	-0.0048	1.0351
8[N88···Pt90]	0.0482	0.1967	-0.0532	0.0511	-0.0021	1.0404
9[N87···Pt90]	0.1412	0.4252	-0.2223	0.1625	-0.0598	1.3683
10[N89···Pt90]	0.1393	0.4246	-0.2185	0.1605	-0.0580	1.3612
11[C10···H118]	0.0051	0.0161	-0.0027	0.0034	0.0007	0.7979

Table 8. QTAIM parameters for intra- and intermolecular interactions in complex F of AFB1 with Pt-embedded pyridinic N-doped graphene.

Critical Point	ρ	$\nabla^2\rho$	V_r	G_r	H_r	$\lvert V_r \rvert / G_r$
1[C63...H115]	0.0072	0.0199	-0.0039	0.0044	0.0005	0.8796
2[C54...H116]	0.0074	0.0226	-0.0041	0.0049	0.0008	0.8368
3[O112...Pt92]	0.0864	0.5488	-0.1466	0.1408	-0.0058	1.0413
4[O113...Pt92]	0.0892	0.5496	-0.1500	0.1426	-0.0075	1.0523
5[O114...C109]	0.0103	0.0477	-0.0077	0.0098	0.0021	0.7867
6[C49...H121]	0.0007	0.0029	-0.0003	0.0005	0.0002	0.5393
7[Pt92...N90]	0.1368	0.4196	-0.2135	0.1575	-0.0560	1.3558
8[Pt92.N91]	0.0460	0.1846	-0.0497	0.0479	-0.0018	1.0378
9[Pt92...N89]	0.1402	0.4004	-0.2154	0.1560	-0.0593	1.3804

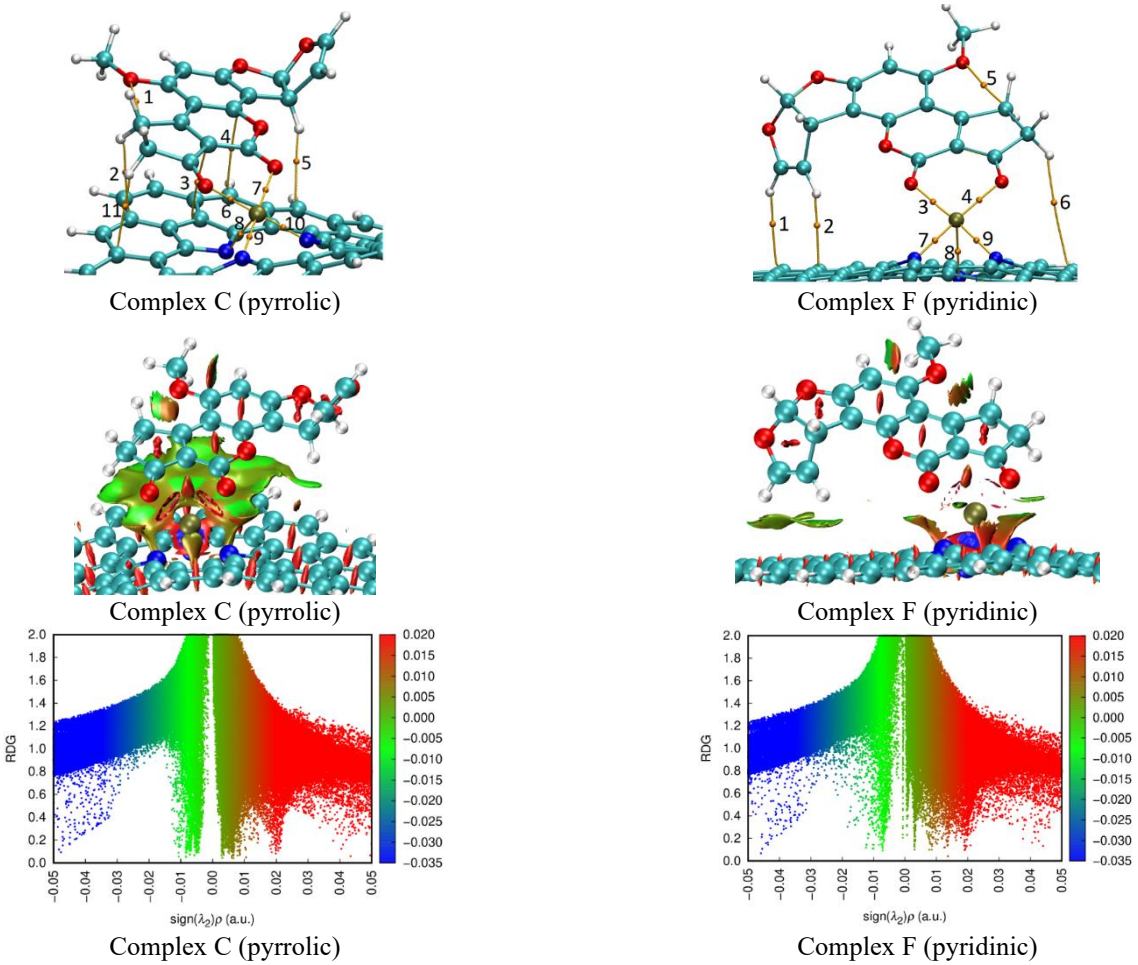

Fig. 12. Topological, non-covalent interactions (NCI), and reduced density gradient (RDG) graphs for pyrrolic (complex C) and pyridinic (complex F) complexes.

4. Conclusion

In this paper, non-periodic density functional theory (DFT) simulations were performed to investigate the interactions of aflatoxin B1 (AFB1) with Pt-embedded pyrrolic and pyridinic N-doped graphene. The results demonstrate that Pt-embedded pyridinic N-doped graphene is a promising candidate for use as a disposable sensor for AFB1 detection. Various configurations of AFB1 adsorbed on both sensors were optimized, and their electronic properties were analyzed.

The DFT calculations revealed that the average band gap change for all optimized configurations is approximately 16% for pyrrolic N-doped graphene and an impressive 810% for pyridinic N-doped graphene. This substantial band gap modulation indicates that Pt-embedded pyridinic N-doped graphene is highly sensitive to AFB1 adsorption, making it suitable for sensing applications. Upon AFB1 adsorption, the electrical conductivity of the Pt-embedded pyridinic N-doped graphene decreases by more than a factor of 10^{20}, effectively transforming the sensor from a conductor to a semiconductor with a band gap of 2.08 eV (about 13 times larger than that of the pristine material). In contrast, the pyrrolic N-doped graphene shows only a 0.5 eV band gap change, indicating its unsuitability as an AFB1 sensor. The average adsorption energy of AFB1 on Pt-embedded pyridinic N-doped graphene is calculated to be 2.7 eV, which significantly increases the recovery time, restricting the material's use to disposable sensor applications.

The high recovery time and the cost associated with sensor fabrication are two major limitations of these sensors from a practical perspective. To provide comprehensive insight into the interactions between AFB1 and the sensors, multiple quantum chemical analyses including Natural Bond Orbital (NBO), Quantum Theory of Atoms in Molecules (QTAIM), Non-Covalent Interaction (NCI), and Reduced Density Gradient (RDG) analyses were employed. Charge transfer studies confirmed that AFB1 acts as an electron donor, while the sensors serve as electron acceptors. The two oxygen atoms in AFB1 and the Pt atom in the sensors are the primary contributors to charge transfer from AFB1 to the N-doped graphene.

Additionally, various quantum chemical descriptors were reported to support future machine learning and artificial intelligence applications aimed at sensor design and optimization. These first-principles data can facilitate the development of advanced smart sensors and support artificial intelligence-driven optimization of sensor performance.

Supplementary files

Supplementary file 1.

Acknowledgements

The authors gratefully acknowledge the support provided by Ardakan and Payame Noor universities.

References

[1] J. W. Bennett, M. Klich, Mycotoxins. *Clin. Microbiol. Rev.*, 16 (2003) 497-516. https://doi.org/10.1128/cmr.16.3.497-516.2003

[2] G. E. Neal, D. L. Eaton, D. J. Judah, A. Verma, Metabolism and toxicity of aflatoxins M_1 and B_1 in human-derived in vitro systems. *Toxicol. Appl. Pharmacol.*, 151 (1998) 152-158. https://doi.org/10.1006/taap.1998.8440

[3] S. Xiulan, Z. Xiaolian, T. Jian, J. Zhou, F. S. Chu, Preparation of gold-labeled antibody probe and its use in immunochromatography assay for detection of aflatoxin B_1. *Int. J. Food Microbiol.*, 99 (2005) 185-194. https://doi.org/10.1016/j.ijfoodmicro.2004.07.021

[4] S. Lian, X. Li, X. Lv, Density functional theory study on the interaction between aflatoxin B_1/M_1 and gold substrate. *Langmuir*, 40 (2024) 1804-1816. https://doi.org/10.1021/acs.langmuir.3c03069

[5] S.-m. Gao, H.-y. Wang, Y.-x. Lin, Surface-enhanced Raman scattering of aflatoxin B_1 on silver by DFT method. *Chin. J. Chem. Phys.*, 27 (2014) 131-136. https://doi.org/10.1063/1674-0068/27/02/131-136

[6] S. Li, K. Qin, Y. Fu, D. He, D. Han, S. Li, et al., Highly efficient removal of aflatoxin B_1 employing a flower-like covalent organic framework-based fiber membrane. *J. Environ. Chem. Eng.*, 11 (2023) 111382. https://doi.org/10.1016/j.jece.2023.111382

[7] M. S. Samuel, V. S. Kirankumar, E. Selvarajan, Fabrication of a metal-organic framework composite for removal of aflatoxin B_1 from water. *J. Environ. Chem. Eng.*, 9 (2021) 104966. https://doi.org/10.1016/j.jece.2020.104966

[8] N. Li, Y. Wang, X. Zhou, C. Hu, X. He, J. Qiao, A novel electrochemical aptasensor based on AuNPs-loaded graphene oxide-polyaniline for sensitive detection of aflatoxin B_1. *J. Solid State Electrochem.*, 28 (2024) 2973-2984. https://doi.org/10.1007/s10008-024-05805-w

[9] M. Xia, X. Yang, T. Jiao, M. Oyama, Q. Chen, X. Chen, Self-enhanced electrochemiluminescence of luminol induced by palladium–graphene oxide for ultrasensitive detection of aflatoxin B_1 in food samples. *Food Chem.*, 381 (2022) 132276. https://doi.org/10.1016/j.foodchem.2022.132276

[10] S. Ramalingam, A. Elsayed, A. Singh, An aflatoxin-M_1 biochip using graphene quantum dot-gold hybrid nanoparticles. *Food Chem.*, 403 (2023) 134302. https://doi.org/10.1016/j.foodchem.2022.134302

[11] S. Mousavi Nodoushan, N. Nasirizadeh, R. Kachuei, A. A. Imani Fooladi, Electrochemical detection of aflatoxin B_1: an aptasensor prepared using graphene oxide and gold nanowires. *Anal. Methods*, 11 (2019) 6033-6042. https://doi.org/10.1039/C9AY01673B

[12] (a) E. Vessally, S. Soleimani-Amiri, A. Hosseinian, L. Edjlali, A. Bekhradnia, A comparative computational study on the BN ring doped nanographenes. *Appl. Surf. Sci.*, 396 (2017) 740-745. https://doi.org/10.1016/j.apsusc.2016.11.019; (b) B. Mohammadi, M. R. Jalali Sarvestani, A comparative

computational investigation on amantadine adsorption on the surfaces of pristine, C-, Si-, and Ga-doped aluminum nitride nanosheets. *J. Chem. Lett.*, 4 (2023) 66–70. https://doi.org/10.22034/jchemlett.2023.388369.1107; (c) F. Najafi, S. S. Alamdar, E. Vaziri, Fullerene (C_{20}) as a sensor for the detection of nordazepam: DFT simulations. *J. Med. Med. Chem.*, 1 (2025) 18–23. https://doi.org/10.22034/jmedchem.2025.526412.1004.

[13] R. Behjatmanesh-Ardakani, R. Rzayev, Pd- and Pt-doped graphene quantum dots for SO_2 adsorption and dissociation: A non-periodic DFT study. *Chem. Rev. Lett.*, 7 (2024) 1022-1030. https://doi.org/10.22034/crl.2024.474971.1412

[14] R. Behjatmanesh-Ardakani, R. Rzayev, Hydrogen assisted SO_2 dissociation on the Pt-doped graphene quantum dot surface: a non-periodic DFT study. *Chem. Rev. Lett.*, 8 (2025) 178-186. https://doi.org/10.22034/crl.2024.489135.1476

[15] (a) M. R. Poor Heravi, A. Bayan, A. M. Evan, E. A. Ghaffar, A. M. Javed, S. Soleimani-Amiri, Molecular simulation of the paracetamol drug interaction with Pt-decorated BC_3 graphene-like nanosheet. *Mol. Simul.*, 48 (2022) 517-525. https://doi.org/10.1080/08927022.2022.2030861; (b) R. Ahmadi, Furazolidone adsorption on the surface of $B_{12}N_{12}$: DFT simulations. *J. Med. Med. Chem.*, 1 (2025) 100–105. https://doi.org/10.22034/jmedchem.2025.547065.1018.

[16] (a) S. J. Hoseyni, A. Karbakhshzadeh, A. Moshtaghi Zonouz, B. Husseen, Computational investigation on interaction between graphene nanostructure BC_3 and antiparkinson drug amantadine: Possible sensing study of BC_3 and its doped derivatives on amantadine. *Chem. Rev. Lett.*, 7 (2024) 380-387. https://doi.org/10.22034/crl.2024.454413.1328; (b) N. Mirderikvand, M. Mahboubi-Rabbani, A DFT study on citalopram adsorption on the surface of $B_{12}N_{12}$. *J. Chem. Technol.*, 1 (2025) 90–95. https://doi.org/10.22034/jchemtech.2025.538393.1015.

[17] A. S. Hessen, N. M. Ahmed Alsultany, H. Bahir, A. H. Adthab, S. Soleimani-Amiri, S. Ahmadi, et al., Adsorption of sulfur mustard on the transition metals (TM = Ti^{2+}, Cr^{2+}, Fe^{2+}, Co^{2+}, Ni^{2+}, Cu^{2+}, Zn^{2+}) porphyrins induced in carbon nanocone (TM-PCNC): Insight from DFT calculation. *J. Mol. Graphics Modell.*, 135 (2025) 108928. https://doi.org/10.1016/j.jmgm.2024.108928

[18] E. Vessally, S. Soleimani-Amiri, A. Hosseinian, L. Edjlali, A. Bekhradnia, The Hartree-Fock exchange effect on the CO adsorption by the boron nitride nanocage. *Physica E*, 87 (2017) 308-311. https://doi.org/10.1016/j.physe.2016.11.010

[19] A. Hosseinian, S. Soleimani-amiri, S. Arshadi, E. Vessally, L. Edjlali, Boosting the adsorption performance of BN nanosheet as an anode of Na-ion batteries: DFT studies. *Phys. Lett. A*, 381 (2017) 2010-2015. https://doi.org/10.1016/j.physleta.2017.04.022

[20] S. Esfahani, J. Akbari, S. Soleimani-Amiri, M. Mirzaei, A. Ghasemi Gol, Assessing the drug delivery of ibuprofen by the assistance of metal-doped graphenes: Insights from density functional theory. *Diamond Relat. Mater.*, 135 (2023) 109893. https://doi.org/10.1016/j.diamond.2023.109893

[21] A. Yadav, A. Taha, Y. A. Abdulsayed, S. M. Saeed, A Density Functional Theory (DFT) study on adsorption of a biological active ethionamide over the surface of a Fe-decorated porphyrin system. *Chem. Rev. Lett.*, 6 (2023) 128-138. https://doi.org/10.22034/crl.2023.387354.1204

[22] F. Mo, W. Ala, C. E. Spano, G. Piccinini, M. Graziano, Y. Ardesi, Single-molecule graphene junction aflatoxin sensors: Chemo-physical insights from ab initio simulations. In: *2024 IEEE 24th International Conference on Nanotechnology (NANO)*, IEEE (2024) 420-423.

[23] I. Nicolás-Vázquez, A. Méndez-Albores, E. Moreno-Martínez, R. Miranda, M. Castro, Role of lactone ring in structural, electronic, and reactivity properties of aflatoxin B_1: A theoretical study. *Arch. Environ. Contam. Toxicol.*, 59 (2010) 393-406. https://doi.org/10.1007/s00244-010-9501-x

[24] F. Kang, Y. Ge, X. Hu, C. Goikavi, M. G. Waigi, Y. Gao, et al., Understanding the sorption mechanisms of aflatoxin B_1 to kaolinite, illite, and smectite clays via a comparative computational study. *J. Hazard. Mater.*, 320 (2016) 80-87. https://doi.org/10.1016/j.jhazmat.2016.08.006

[25] X. Cai, Q. Yang, Y. Tong, S. Zhang, M. Wang, G-C_3N_5 nanotube as a promising candidate for adsorption and inactivation of aflatoxin B_1: A first-principles study. *Surf. Interfaces*, 38 (2023) 102868. https://doi.org/10.1016/j.surfin.2023.102868

[26] F. Ashtari Mahini, P. Niknam Rad, Aflatoxin M_1 interaction with $B_{12}N_{12}$ nanocage: DFT studies. *Int. J. New Chem.*, 10 (2023) 299-316. https://doi.org/10.22034/ijnc.2023.713326

[27] N. Khalaj Zeighami, D. Abdolkhani, Fullerene (C_{20}) as a sensor and adsorbent for aflatoxin M_1: DFT studies. *Int. J. New Chem.*, 11 (2024) 139-149. https://doi.org/10.22034/ijnc.2024.715907

[28] B. Hammer, L. B. Hansen, J. K. Nørskov, Improved adsorption energetics within density-functional theory using revised Perdew-Burke-Ernzerhof functionals. *Phys. Rev. B*, 59 (1999) 7413-7421. https://doi.org/10.1103/PhysRevB.59.7413

[29] V. Blum, R. Gehrke, F. Hanke, P. Havu, V. Havu, X. Ren, et al., Ab initio molecular simulations with numeric atom-centered orbitals. *Comput. Phys. Commun.*, 180 (2009) 2175-2196. https://doi.org/10.1016/j.cpc.2009.06.022

[30] S. Kokott, F. Merz, Y. Yao, C. Carbogno, M. Rossi, V. Havu, et al., Efficient all-electron hybrid density functionals for atomistic simulations beyond 10 000 atoms. *J. Chem. Phys.*, 161 (2024) 034106. https://doi.org/10.1063/5.0208103

[31] A. Marek, V. Blum, R. Johanni, V. Havu, B. Lang, T. Auckenthaler, et al., The ELPA library: scalable parallel eigenvalue solutions for electronic structure theory and computational science. *J. Phys.: Condens. Matter*, 26 (2014) 213201. https://doi.org/10.1088/0953-8984/26/21/213201

[32] V. Havu, V. Blum, P. Havu, M. Scheffler, Efficient O(N) integration for all-electron electronic structure calculation using numeric basis functions. *J. Comput. Phys.*, 228 (2009) 8367-8379. https://doi.org/10.1016/j.jcp.2009.08.008

[33] Z.-Y. Qiu, J.-S. Dang, Mechanistic studies on defective hBN-supported metal-nonmetal synergistic catalysis for

urea electrosynthesis. *Appl. Surf. Sci.*, 679 (2025) 161230. https://doi.org/10.1016/j.apsusc.2024.161230

[34] R. Behjatmanesh-Ardakani, A. Heydari, Molecular and dissociative adsorption of tetrachlorodibenzodioxin on M-doped graphenes (M = B, Al, N, P): pure DFT and DFT + VdW calculations. *J. Mol. Model.*, 26 (2020) 164. https://doi.org/10.1007/s00894-020-04387-4

[35] R. Behjatmanesh-Ardakani, E. M. Bahalkeh, V. Moeini, A mechanistic periodic DFT study of CH, CO, and OH dissociations in methanol: M-doped carbon nanotubes (M=Pt, B, Al, N, P) versus Pt(100), Pt(110) and Pt(111) surfaces. *Mol. Catal.*, 512 (2021) 111781. https://doi.org/10.1016/j.mcat.2021.111781

[36] R. Behjatmanesh-Ardakani, Periodic hybrid-DFT study on the N-doped TiO_2(001) nanotubes as solar water splitting catalysts: A comparison with the rutile and anatase bulk phases. *Int. J. Hydrogen Energ.*, 48 (2023) 35584-35598. https://doi.org/10.1016/j.ijhydene.2023.05.352

[37] R. Behjatmanesh-Ardakani, A. Moradzadeh, Dual surface doping of Co+N in the anatase TiO_2(100) for water splitting process. *Chem. Rev. Lett.*, 7 (2024) 17-19. https://doi.org/10.22034/crl.2024.435210.1278

[38] Y. Zhao, D. G. Truhlar, The M06 suite of density functionals for main group thermochemistry, thermochemical kinetics, noncovalent interactions, excited states, and transition elements: two new functionals and systematic testing of four M06-class functionals and 12 other functionals. *Theor. Chem. Acc.*, 120 (2008) 215-241. https://doi.org/10.1007/s00214-007-0310-x

[39] M. J. Frisch, G. W. Trucks, H. B. Schlegel, G. E. Scuseria, M. A. Robb, J. R. Cheeseman, et al., *Gaussian 16, Revision A.01*. Gaussian, Inc., Wallingford, CT (2016).

[40] E. D. Glendening, C. R. Landis, F. Weinhold, NBO 6.0: Natural bond orbital analysis program. *J. Comput. Chem.*, 34 (2013) 1429-1437. https://doi.org/10.1002/jcc.23266

[41] T. Lu, F. Chen, Multiwfn: A multifunctional wavefunction analyzer. *J. Comput. Chem.*, 33 (2012) 580-592. https://doi.org/10.1002/jcc.22885

[42] W. Humphrey, A. Dalke, K. Schulten, VMD: Visual molecular dynamics. *J. Mol. Graphics*, 14 (1996) 33-38. https://doi.org/10.1016/0263-7855(96)00018-5

[43] R. Dennington, T. A. Keith, J. M. Millam, *GaussView, Version 5.0*. Semichem Inc., Shawnee Mission, KS (2016).

[44] R. G. Parr, R. G. Pearson, Absolute hardness: companion parameter to absolute electronegativity. *J. Am. Chem. Soc.*, 105 (1983) 7512-7516. https://doi.org/10.1021/ja00364a005

[45] R. G. Parr, R. A. Donnelly, M. Levy, W. E. Palke, Electronegativity: The density functional viewpoint. *J. Chem. Phys.*, 68 (1978) 3801-3807. https://doi.org/10.1063/1.436185

[46] R. G. Parr, L. v. Szentpály, S. Liu, Electrophilicity index. *J. Am. Chem. Soc.*, 121 (1999) 1922-1924. https://doi.org/10.1021/ja983494x

[47] Y. Li, Y. Xu, X. Li, The sensing mechanism of HCHO gas sensor based on transition metal doped graphene: Insights from DFT study. *Sens. Actuators A Phys.*, 338 (2022) 113460. https://doi.org/10.1016/j.sna.2022.113460

[48] R. F. W. Bader, *Atoms in Molecules: A Quantum Theory*. Clarendon Press, Oxford (1994).

[49] C. Guerra, J. Burgos, L. Ayarde-Henríquez, E. Chamorro, Formulating reduced density gradient approaches for noncovalent interactions. *J. Phys. Chem. A*, 128 (2024) 6158-6166. https://doi.org/10.1021/acs.jpca.4c01667